Supplementary Information

Stepwise Construction of Ag_{29} Nanocluster-Based Hydrogen Evolution Electrocatalysts

Honglei Shen,[+a] Qingtao Zhu,[+a] Jiawei Xu,[a] Kun Ni,*[c] Xiao Wei,[a] Yuanxin Du,*[b] Shan Gao,*[a] Xi Kang*[a] and Manzhou Zhu[a]

[a] Department of Chemistry and Centre for Atomic Engineering of Advanced Materials, Anhui Province Key Laboratory of Chemistry for Inorganic/Organic Hybrid Functionalized Materials, Anhui University, Hefei 230601, P. R. China.

E-mail: shangao@ahu.edu.cn (S.G.); kangxi_chem@ahu.edu.cn (X.K.)

[b] Key Laboratory of Structure and Functional Regulation of Hybrid Materials, Anhui University, Ministry of Education, Hefei 230601, P. R. China.

E-mail: duyuanxin@ahu.edu.cn (Y.D.)

[c] CAS Key Laboratory of Materials for Energy Conversion & Department of Materials Science and Engineering & iChEM, University of Science and Technology of China, Hefei, 230026, P. R. China.

E-mail: nikun@ustc.edu.cn (K.N.)

+*These authors contributed equally to this work.*

This Supporting Information includes:

Experimental Section

1. Materials

Silver nitrate ($AgNO_3$, 99.5% metal basis), hexachloroplatinic acid ($H_2PtCl_6{\cdot}6H_2O$, 99.9% metals basis), manganous chloride ($MnCl_2$, 97% metal basis), iron dichloride ($FeCl_2$, 97% metal basis), cobaltous chloride ($CoCl_2$, 97% metal basis), nickel chlorite ($NiCl_2$, 97% metal basis), 1,3- benzenedithiol (BDT, $C_6S_2H_6$, 99%), 1,3,5-benzenetrithiol (BTT, $C_6S_3H_6$, 99%), triphenylphosphine (PPh_3, $C_{18}H_{15}P$, 99%), sodium borohydride ($NaBH_4$, 99%), methylene chloride (CH_2Cl_2, HPLC grade), methanol (CH_3OH, HPLC grade), ethyl ether ($(CH_3)_2O$,HPLC grade), N,N-dimethylformamide (DMF, HPLC grade) were purchased from Sigma-Aldrich. Cabot vulcan XC-72R (XC-72R, mesopor, >60%, OD: 2-4 nm) was purchased from Carbot Co. All reagents were used without further purification.

2. Synthesis

2.1 Synthesis of MAg_{28}-BDT (M = Ag, Pt)

The Ag_{29}-BDT and Pt_1Ag_{28}-BDT were synthesized via previously reported methods.[1, 2]

2.2 Synthesis of Pt_1Ag_{28}-BTT

The Pt_1Ag_{28}-BTT nanocluster was prepared by reacting the $[Pt_1Ag_{28}(S\text{-}Adm)_{18}(TPP)_4]^{2+}$ nanocluster (abbreviated as Pt_1Ag_{28}-AdmSH) with BTT ligands. The Pt_1Ag_{28}-AdmSH was obtained via a previously reported method.[3] Specifically, 100 mg of Pt_1Ag_{28}-AdmSH was dissolved in 10 mL of CH_2Cl_2 under vigorous stirring, and then 20 mg of BTT was added. After 10 minutes, 10 mg of PPh_4Br (dissolved in 1 mL of CH_3OH) was added, and the reaction was continued for another 2 hours. After centrifugation, the dark orange precipitate was washed several times with CH_3OH to remove the excess thiol ligands. Then, 5 mL of DMF was used to extract the obtained Pt_1Ag_{28}-BTT nanocluster. The Pt_1Ag_{28}-BTT nanocluster was crystallized via a gas phase diffusion method by diffusing ethyl ether into the DMF solution of the nanocluster for three days.

2.3 Synthesis of Pt_1Ag_{28}-BTT-M(50) (M = Mn, Fe, Co, Ni)

2 mg of the Pt_1Ag_{28}-BTT nanocluster was dissolved in 1 mL of DMF, and 50 μL of $MnCl_2$, $FeCl_2$, $CoCl_2$, or $NiCl_2$ solutions (dissolved in DMF; 35.2 mg/mL) was dropped into the cluster solution. The obtained solution was stirred for 10 minutes and then stood for 1h to completely construct S-M interactions on the surface of Pt_1Ag_{28}-BTT. 100 mL of ethyl ether was used to wash the unreacted compositions. Finally, the Pt_1Ag_{28}-BTT-M(50) (M= Mn, Fe, Co, Ni) was obtained.

2.4 Synthesis of Pt_1Ag_{28}-BTT-Mn(X) (X represents the molar ratio of nanoclusters to Mn^{2+})

2 mg of the Pt_1Ag_{28}-BTT nanocluster was dissolved in 1mL of DMF. Then, 1 μL, 5 μL, 10 μL, and 50 μL of $MnCl_2$ solution (dissolved in DMF; 35.17 mg/mL) was dropped into the former solution. The obtained solution was stirred for 10 minutes and then stood for 1h to completely construct S-M interactions on the surface of Pt_1Ag_{28}-BTT. 100 mL of ethyl ether was used to wash the unreacted compositions. Finally, the Pt_1Ag_{28}-BTT-Mn(1), Pt_1Ag_{28}-BTT-Mn(5), Pt_1Ag_{28}-BTT-Mn(10), and Pt_1Ag_{28}-BTT-Mn(50) was obtained.

2.5 Synthesis of all series of M_{29} electrocatalysts (10 wt.% loaded in XC-72R)

20 mg of XC-72R were suspended in 2 mL of the mixed solvent of EtOH and DMF (*V*:*V* = 1:1), and the obtained solution was dispersed via ultrasonic for 30 minutes. Next, 2 mg of nanoclusters (dissolved in 1 mL of DMF) was slowly added to the suspensions and kept stirring for 8 h. The suspensions were centrifuged at high speed (rpm = 10000 r/min) to get precipitates and then washed by DMF and EtOH several times. Finally, the M_{29} electrocatalysts were collected by decompression drying.

3. Characterization

The UV-vis absorption spectra of nanoclusters were recorded using an Agilent 8453 diode array spectrometer. Electrospray ionization mass spectrometry (ESI-MS) measurements were performed using a MicrOTOF-QIII high-resolution mass spectrometer. For preparing the ESI samples, nanoclusters were dissolved in DMF (0.1 mg/mL) and diluted (V/V = 1:1) using CH_3OH. X-ray photoelectron spectroscopy (XPS) measurements were performed on a Thermo ESCALAB 250 instrument configured with a monochromatized Al Kα (1486.8 eV) 150 W X-ray source, 0.5 mm circular spot size, flood gun to counter charging effects, and analysis chamber base pressure lower than 1×10^{-9} mbar. Inductively coupled plasma-atomic emission spectrometry (ICP-AES) measurements were performed on an Atomscan Advantage instrument made by Thormo Jarrell Ash Corporation (USA). The nanoclusters were digested with concentrated nitric acid, and the concentration of the nanoclusters was set to ~ 0.1 mg/L. Dynamic light scattering (DLS) was performed with a Malvern Zetasizer Nano ZS instrument. The DLS result of each nanocluster was repeated 100 times to remove the error. Transmission electron microscopy (TEM) was conducted on a JEM-2100 microscope with an accelerating voltage of 200 kV. Energy-dispersive X-ray spectroscopy (EDS) analyses were performed on a JEOL JEM-2100F FEG TEM operated at 200 kV. The Pt_1Ag_{28}-BTT-Mn(10) catalyst was imaged with an aberration-corrected HAADF-STEM (high angle annular dark field scanning transmission electron microscope) after the solvent that contained Pt_1Ag_{28}-BTT-Mn(10) catalyst was drop-cast onto ultrathin carbon film TEM grids. The microscope employed was a FEI Themis Z. The electron beam energy was 200 kV.

4. X-ray crystallography

The data collection for single-crystal X-ray diffraction of Pt_1Ag_{28}-BTT was carried out on a Stoe Stadivari diffractometer under nitrogen flow, using graphite-monochromatized Cu Kα radiation (λ = 1.54186 Å). Data reductions and absorption corrections were performed using the SAINT and SADABS programs, respectively. The electron density was squeezed by Platon. The structure was solved by direct methods and refined with full-matrix least squares on F2 using the SHELXTL software package. All non-hydrogen atoms were refined anisotropically, and all the hydrogen atoms were set in geometrically calculated positions and refined isotropically using a riding model. The CCDC number of the Pt_1Ag_{28}-BTT nanocluster is 2225417.

5. Electrochemical measurements

All electrochemical test were implemented in a three-electrode system at an electrochemical station (CHI760E). The graphite rod and the saturated Ag/AgCl electrode (Hg/HgO electrode for alkaline HER) served as the count electrode and the reference electrode, respectively. The catalyst ink was prepared as follows: 3 mg catalyst was dispersed in 0.6 mL of solution containing 590 μL absolute ethyl alcohol and 10 μL of 5 wt% Nafion solution, followed by ultrasonication for 30 min to form homogeneous ink. To prepare the working electrode, the ink was transferred onto the carbon paper (area of working electrode: 0.2 cm^2). The ink was blow-dried by N_2 gas, a working electrode was obtained with a catalyst loading of 0.2 mg/cm^2. Moreover, 0.5 M H_2SO_4 and 1 M KOH were used as the acid and alkali electrolyte for HER, respectively.

The polarization curves were obtained by sweeping the potential from 0 to −0.7 V versus Ag/AgCl at room temperature with a sweep rate of 5 mV/s in N_2-saturated 0.5 M H_2SO_4 solution and 1M KOH solution. It is worth noting that all polarization curves were corrected with 85% internal resistance (IR) drop compensation manually, and all potentials were referenced by reversible hydrogen electrodes (RHE). All the potentials shown in our tests were calibrated and transformed to RHE: E(RHE) = E(Ag/AgCl) + 0.2147 V and E(RHE) = E(Ag/AgCl) + 0.9642 V for acidic and alkaline conditions, respectively. Tafel slopes were calculated from the corresponding linear sweep voltammetry curves. Electrochemical impedance spectroscopy (EIS) measurements were carried out in a frequency range of 100 kHz to 0.01 Hz with an amplitude of 5 mV at the overpotential of 10 mA/cm^2. The electrochemical active surface area (ECSA) of samples was estimated using a simple cyclic voltammetry (CV) method. The current density was measured from 20 mV to 180 mV with 40 mV/s increasing, and the voltage window (vs. RHE) was from 0.25 V to 0.35 V (0.5 M H_2SO_4) and 0.725 V to 0.825 V (1 M KOH). The ECSA is determined by dividing the C_{dl} with the specific capacitance, C_s, assuming a specific capacitance of 60 μF/cm^2. The roughness factor was determined by dividing this ECSA with the geometric area of the electrode.[4]

6. Mass activity calculation

The following formula was used to calculate the mass activity of the samples:

$$\text{Mass activity} = \frac{\text{Current density}}{\text{percent of metal mass} \times \text{catalyst loading of working electrode}}$$

The noble metal contents of the four nanoclusters listed below were measured by inductively coupled plasma–atomic emission spectroscopy (ICP-AES):

Pt_1Ag_{28}-BTT-Mn(10): Ag: 49.4%

Pt_1Ag_{28}-BTT: Ag: 52.0%

Pt_1Ag_{28}-BDT: Ag: 50.8%

Ag_{29}-BDT: Ag: 53.4%

7. Computational methods

Density functional theory (DFT)[5] calculations were performed using the Vienna ab initio simulation package (VASP) software[6] with Generalized Gradient Approximation (GGA)[7] and Perdew−Burke−Ernzerhof (PBE)[8] functional. The DFT-D3[9,10] method with Becke-Jonson damping was utilized for vdW corrections. To prevent interaction between periodic lattices, a vacuum layer larger than 10 Å was employed. Self-consistent field (SCF) iteration energy tolerance was set to 1×10^{-5} eV, and force tolerance was set to 0.05 eV/Å for geometry optimizations. A plane wave basis set with an energy cutoff of 400 eV was used, with unrestricted spin for all calculations. A gamma-centered 1×1×1 K point was sampled for all cluster models.

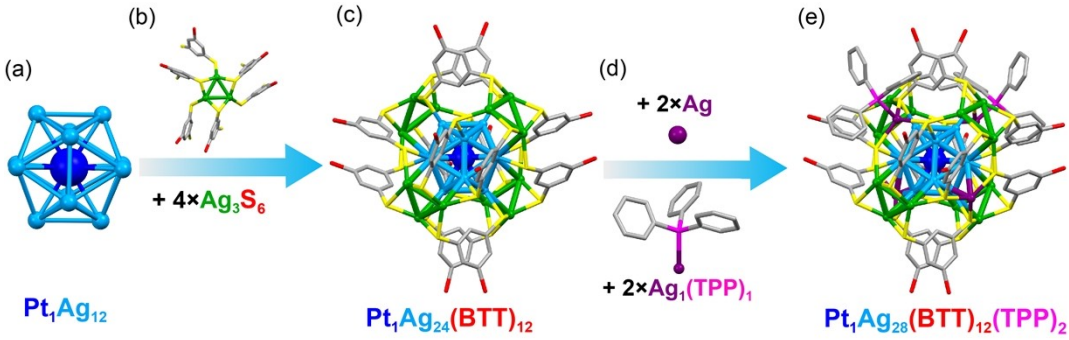

Figure S1. Structural anatomy of Pt_1Ag_{28}-BTT nanoclusters. Color legends: blue sphere, Pt; light blue/green/purple sphere, Ag; yellow sphere, connected S; red sphere, active S; magenta sphere, P; gray sphere, C. All H atoms are omitted for clarity.

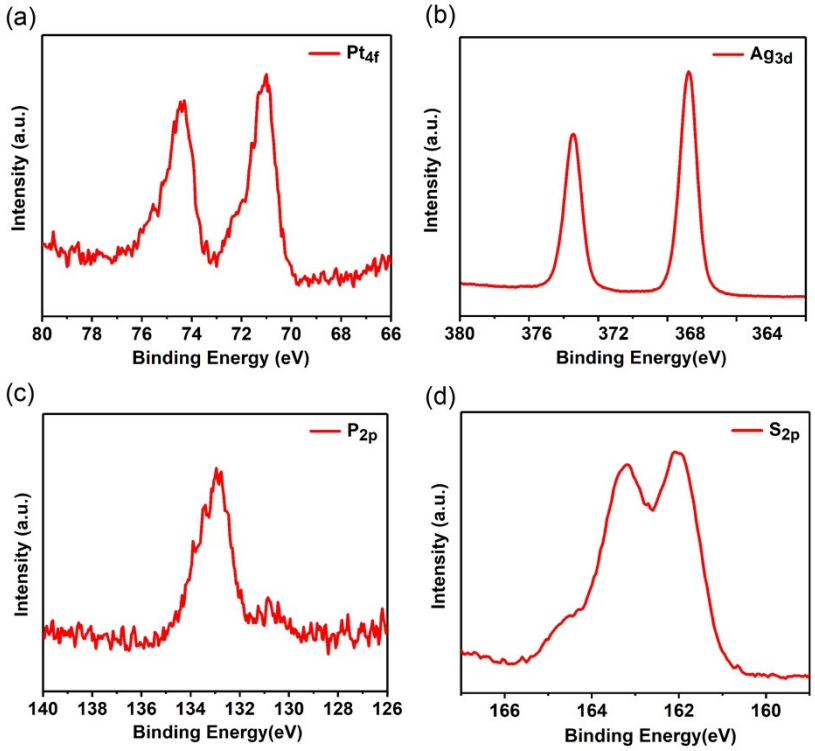

Figure S2. XPS spectra of the $Pt_1Ag_{28}(BTT)_{12}(TPP)_2$ nanocluster. (a) Pt 4f, (b) Ag 3d, (c) P 2p and (d) S 2p.

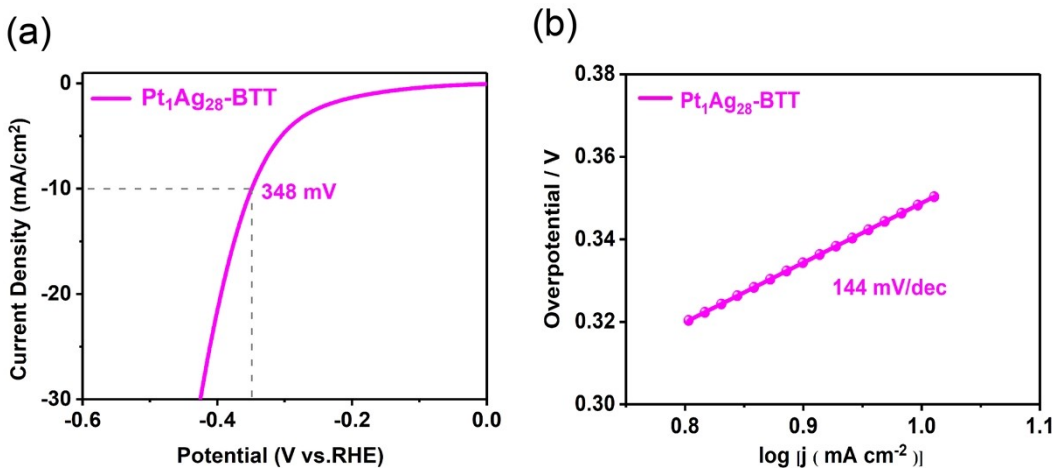

Figure S3. (a) LSV curve and (b) Tafel slope of the Pt_1Ag_{28}-BTT catalyst (loaded on XC-72R), measured in 0.5 M H_2SO_4 solution.

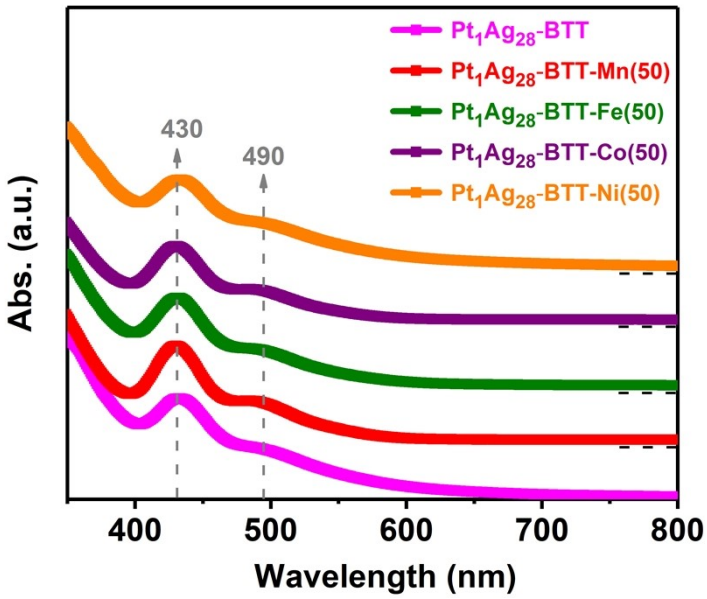

Figure S4. UV-vis comparison of Pt_1Ag_{28}-BTT and Pt_1Ag_{28}-BTT-M(50), these species have added different metal cations (Mn^{2+}, Fe^{2+}, Co^{2+}, and Ni^{2+}) to Pt_1Ag_{28}-BTT system.

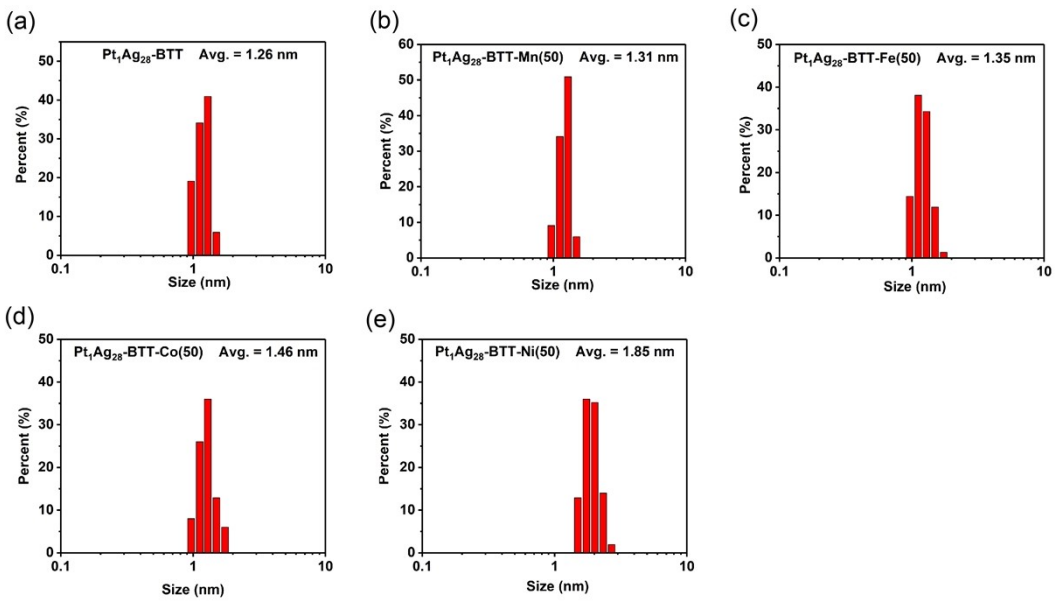

Figure S5. DLS results of before and after adding metal cations to Pt_1Ag_{28}-BTT system. (a) Pt_1Ag_{28}-BTT; (b) Pt_1Ag_{28}-BTT-Mn(50); (c) Pt_1Ag_{28}-BTT-Fe(50); (d) Pt_1Ag_{28}-BTT-Co(50); (e) Pt_1Ag_{28}-BTT-Ni(50). All the Pt_1Ag_{28}-BTT-M(50) were measured in DMF solution.

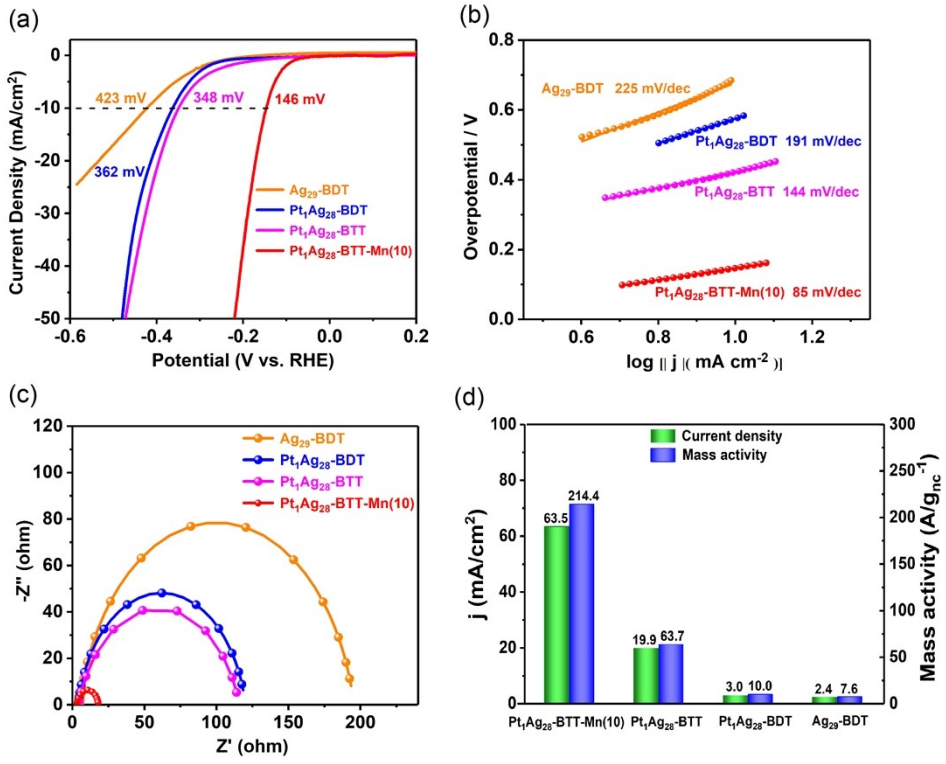

Figure S6. HER ability comparison of a series of M_{29} nano-catalysts in 0.5 M H_2SO_4 solution. Electrochemical measurement of (a) LSV curves; (b) Tafel slopes; and (c) EIS Nyquist plots; (d) Bar diagram of the current density and mass activity comparison for M_{29} nano-catalysts at the overpotential of 0.25 V versus RHE.

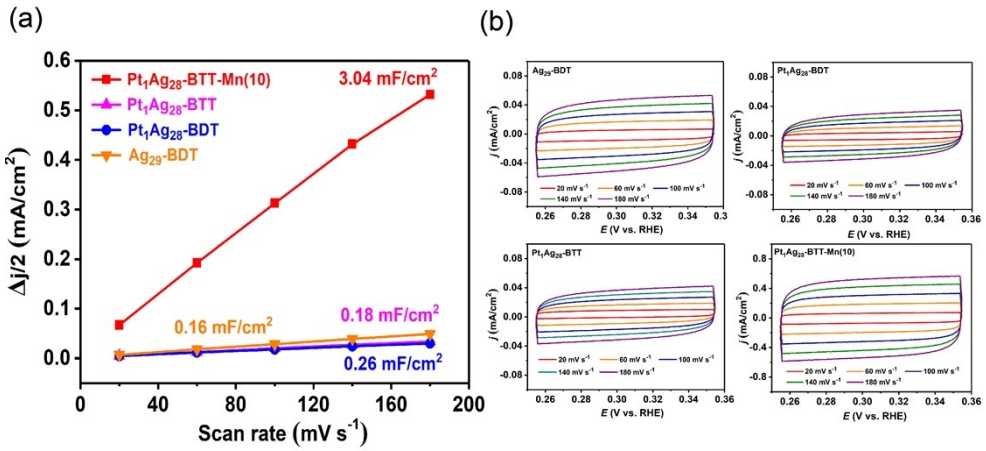

Figure S7. (a) The calculated C_{dl} for M_{29} nano-catalysts in 0.5 M H_2SO_4 solution; (b) The corresponding CV curves of Ag_{29}-BDT, Pt_1Ag_{28}-BDT, Pt_1Ag_{28}-BTT and Pt_1Ag_{28}-BTT-Mn(10) at different scan rates of 20, 60, 100, 140, and 180 mV s^{-1} in 0.5 M H_2SO_4 solution

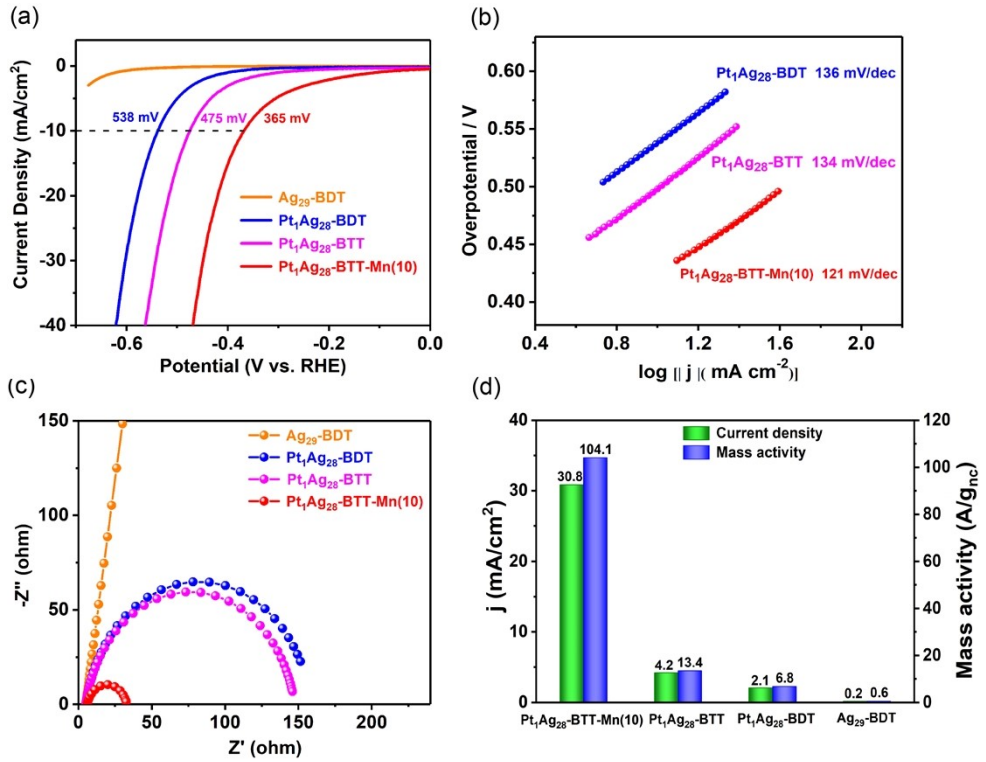

Figure S8. HER ability comparison a series of M_{29} nano-catalysts in 1 M KOH solution. Electrochemical measurement of (a) LSV curves; (b) Tafel slopes; and (c) EIS Nyquist plots; (d) Bar diagram of the current density and mass activity comparison for M_{29} nano-catalysts at the overpotential of 0.45 V versus RHE.

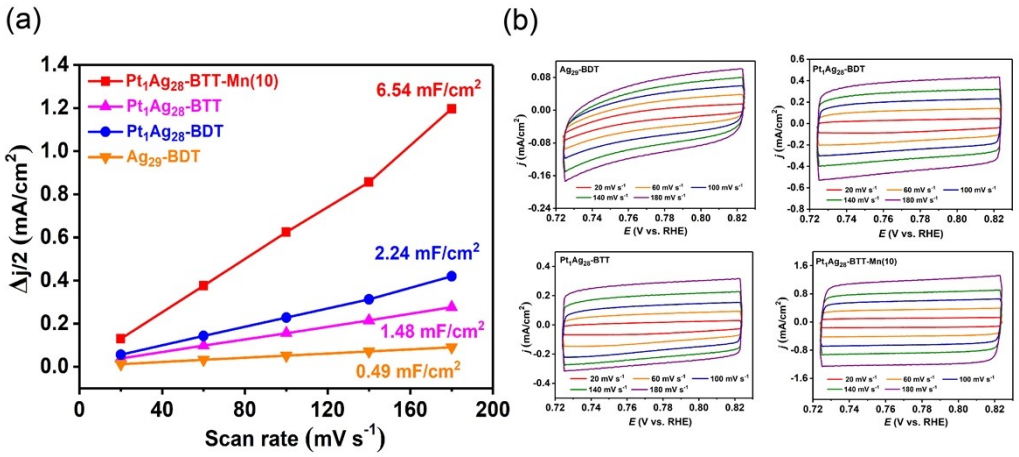

Figure S9. (a) The calculated C_{dl} for M_{29} nano-catalysts in 1 M KOH solution; (b) The corresponding CV curves of Ag_{29}-BDT, Pt_1Ag_{28}-BDT, Pt_1Ag_{28}-BTT and Pt_1Ag_{28}-BTT-Mn(10) at different scan rates of 20, 60, 100, 140, and 180 mV s^{-1} in 1 M KOH solution.

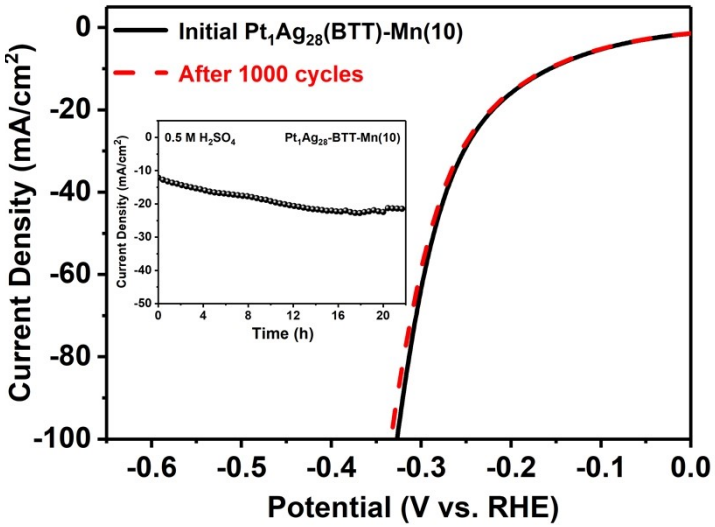

Figure S10. LSV curves of Pt_1Ag_{28}-BTT-Mn(10) before and after 1000 CV cycles sweeping (the inset shows the durability tests of Pt_1Ag_{28}-BTT-Mn(10) at a constant current density of 12 mA/cm^2 for 22 h) in 0.5 M H_2SO_4.

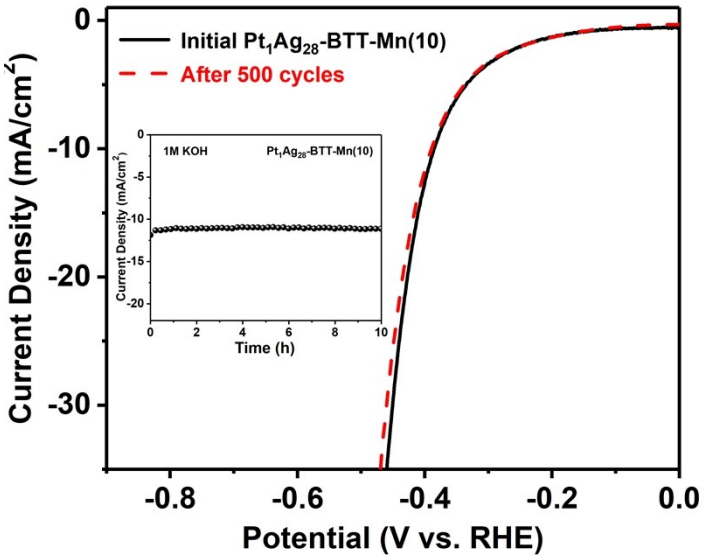

Figure S11. LSV curves of Pt_1Ag_{28}-BTT-Mn(10) before and after 500 CV cycles sweeping (the inset shows the durability tests of Pt_1Ag_{28}-BTT-Mn(10) at a constant current density of 12 mA/cm^2 for 10 h) in 1 M KOH.

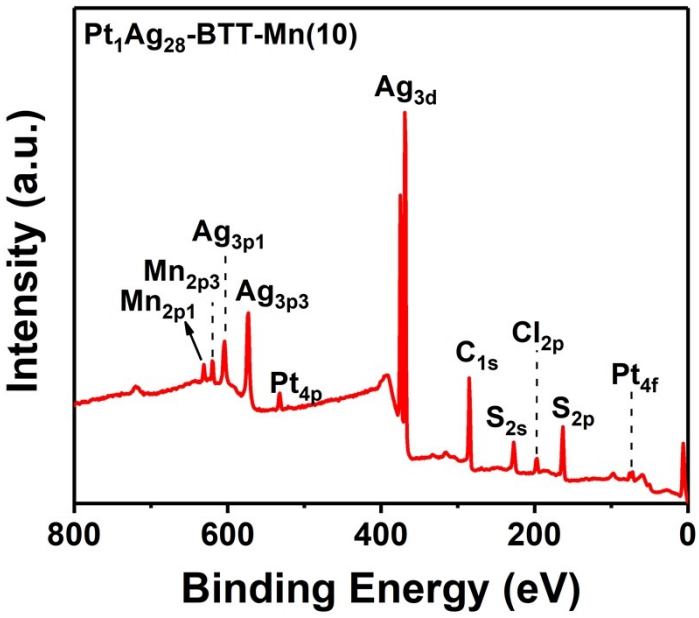

Figure S12. Total XPS spectra of Pt_1Ag_{28}-BTT-Mn(10).

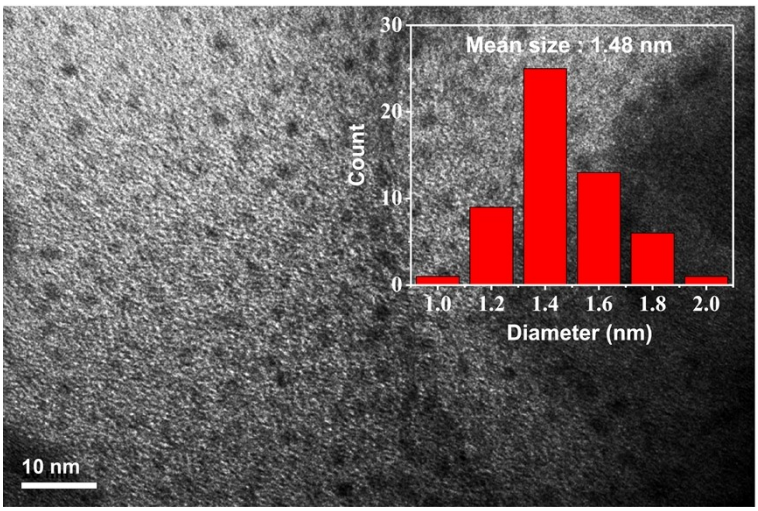

Figure S13. TEM image of Pt_1Ag_{28}-BTT-Mn(10) catalyst (loaded on XC-72R); inset: size distribution of Pt_1Ag_{28}-BTT-Mn(10).

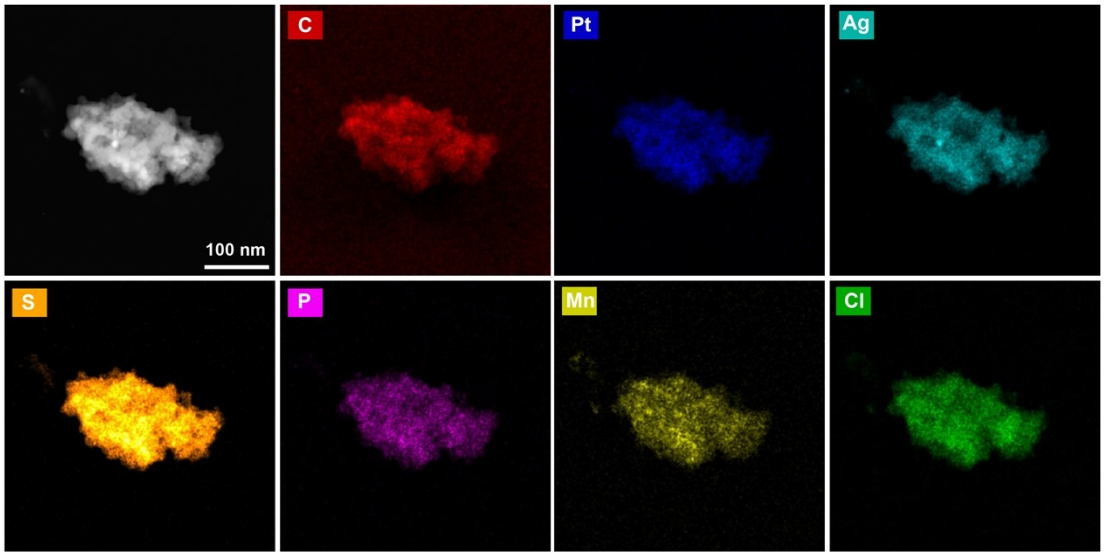

Figure S14. HAADF-STEM imaging and EDS-mapping of Pt_1Ag_{28}-BTT-Mn(10) catalyst.

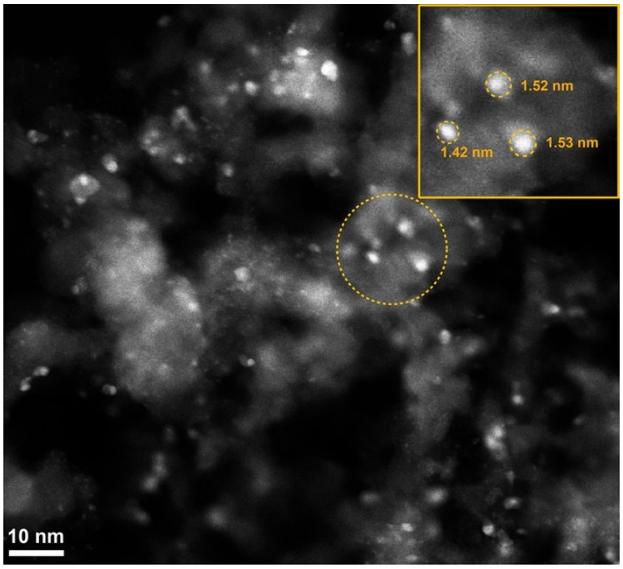

Figure S15. Aberration-corrected HAADF-STEM image of Pt_1Ag_{28}-BTT-Mn(10) ; inset: the magnified image of Pt_1Ag_{28}-BTT-Mn(10).

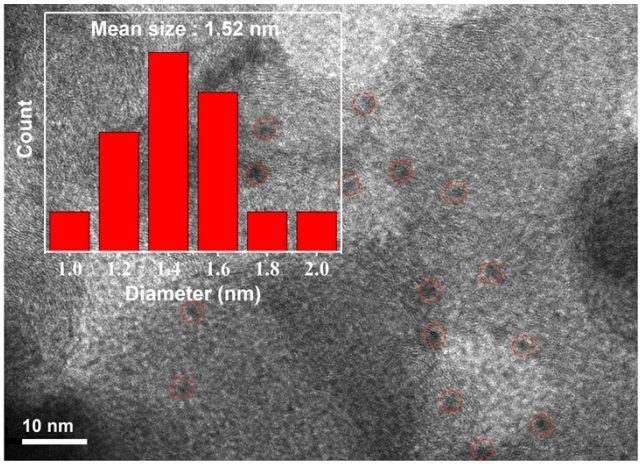

Figure S16. TEM image of Pt_1Ag_{28}-BTT-Mn(10) catalyst after HER; inset: size distribution of Pt_1Ag_{28}-BTT-Mn(10).

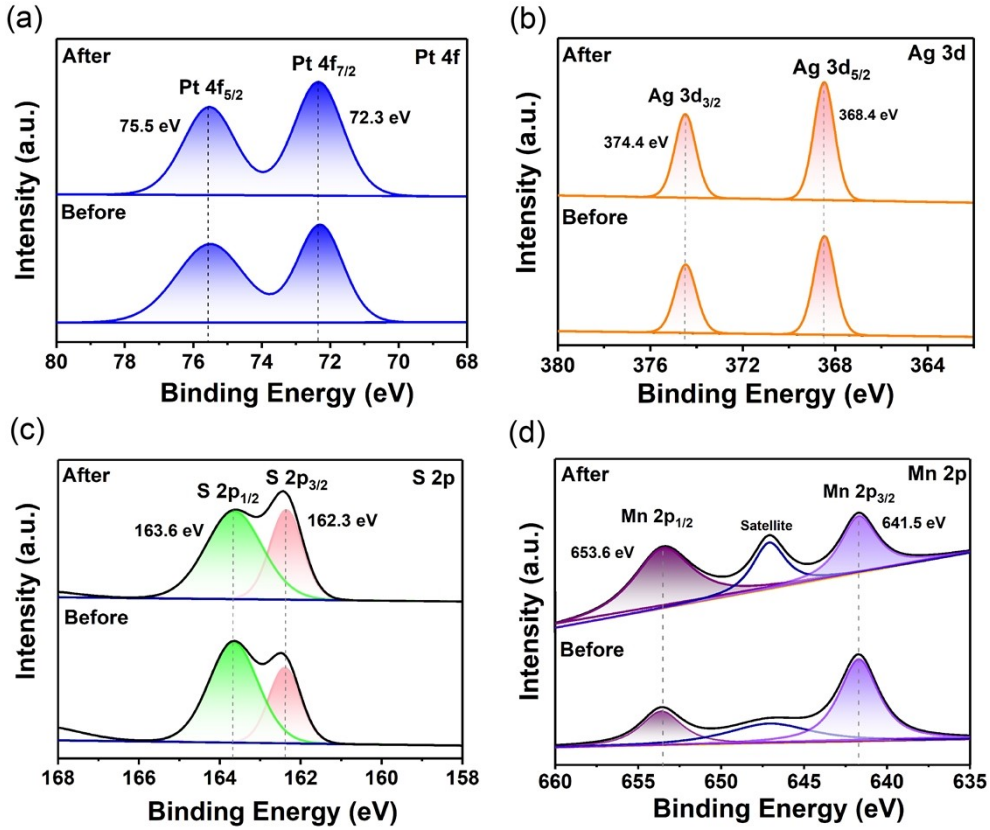

Figure S17. XPS spectra of Pt_1Ag_{28}-BTT-Mn(10) catalyst before and after HER testing. (a) Pt 4f, (b) Ag 3d, (c) S 2p, and (d) Mn 2p.

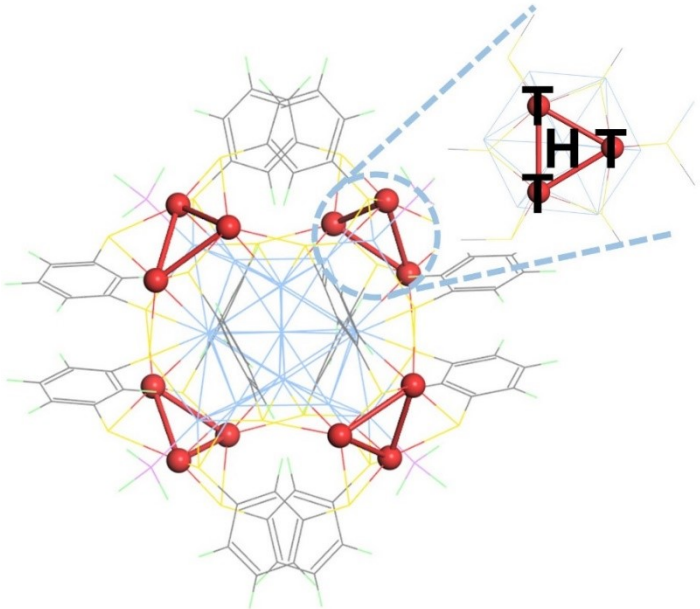

Figure S18. The geometry model and the illustration of adsorption sites of Ag_{29}-BDT.

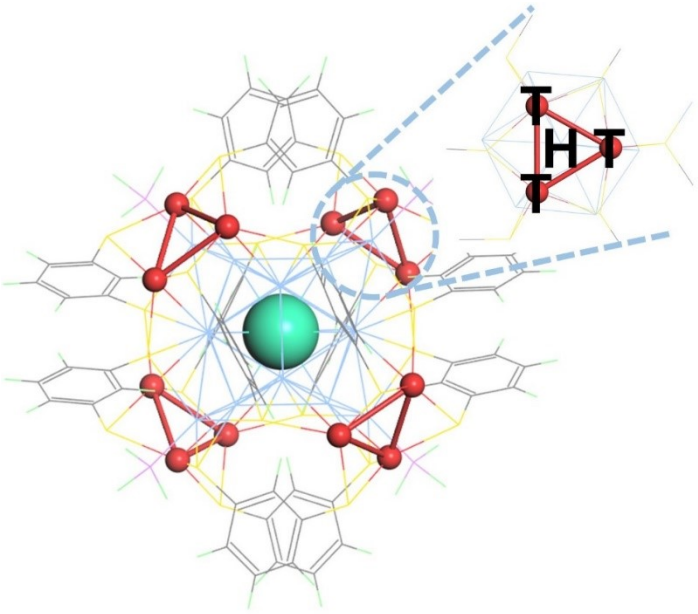

Figure S19. The geometry model and the illustration of adsorption sites of Pt_1Ag_{28}-BDT.

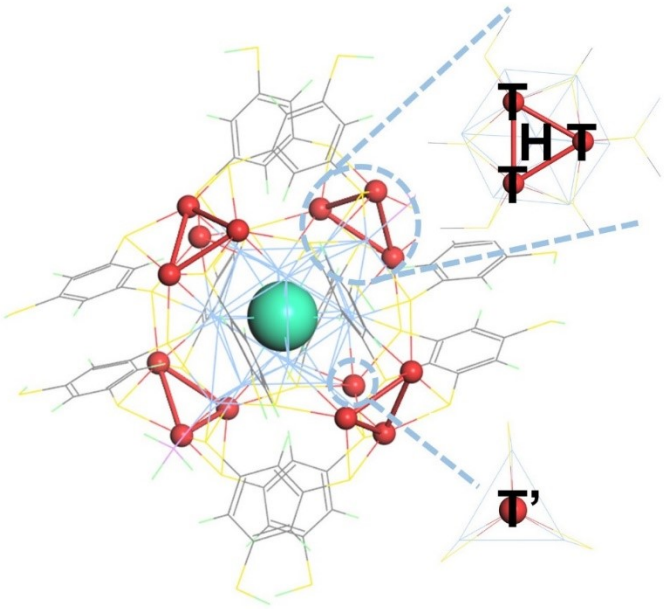

Figure S20. The geometry model and the illustration of adsorption sites of Pt_1Ag_{28}-BTT.

Table S1. Comparisons of HER performance for Au/Ag/Pt-based catalysts tested in 0.5 M H_2SO_4 and 1.0 M KOH.

Catalysts	Electrolyte	η(10 mA/cm²)	Tafel slope (mV/dec)	Exchange current density (A/cm²)	Ref
Pt_1Ag_{28}-BTT-Mn(10)/C	0.5 M H_2SO_4	146	85	9.50×10^{-4}	This work
$Au_{36}Ag_2(SC_{10}H_{15})_{18}$/C	0.5 M H_2SO_4	250	125	2.24×10^{-4}	11
Au_{11}@MoS_2	0.5 M H_2SO_4	292	63	NA	12
Au_2Pd_6/MoS_2	0.5 M H_2SO_4	232	67	9.88×10^{-6}	13
$Au_{25}(PET)_{18}/MoS_2$	0.5 M H_2SO_4	287	79.3	NA	14
Ag NCs/MoS_2	0.5 M H_2SO_4	230	106	NA	15
PtO_x/TiO_2	0.5 M H_2SO_4	150	40	6.30×10^{-5}	16
Pt-Ag/SiNW	0.5 M H_2SO_4	190	54	6.80×10^{-6}	17
Rh-Ag/SiNW	0.5 M H_2SO_4	120	51	7.58×10^{-5}	17
$AgPt/C_3N_4$	0.5 M H_2SO_4	308	120	NA	18
$NiAg_{24}$ NCs	1 M KOH	270	58	NA	19
Au@Pd IHNPs	1 M KOH	659	169	NA	20

Table S2. EXAFS fitting parameters at the Cu K-edge for various samples

Sample	Shell	N^a	R(Å)^b	σ^2(Å^2)^c	ΔE_0(eV)^d	R factor
Mn foil	Mn-Mn	2.3	2.66	0.0070	6.77	0.0252
Mn_2O_3	Mn-O	2.7	1.92	0.0005	-9.80	0.0223
MnO	Mn-O	6.0	1.91	0.0047	0.68	0.0110
Sample	Mn-S	4.0	2.087	0.0026	1.17	0.0242

$^a N$: coordination numbers; $^b R$: bond distance; $^c \sigma^2$: Debye-Waller factors; ^{d} ΔE_0: the inner potential correction. R factor: goodness of fit. S_0^2 was set to 0.55, according to the experimental EXAFS fit of metal foil by fixing Mn as the known crystallographic value.

Table S3. Theoretical and experimental of molar ratio of $n_{cluster}$: n_{Mn} (measured by ICP-AES).

Mole ratio of $n_{cluster}$: n_{Mn}	
Theoretical	Experimental
1 : 1	1 : 0.82
1 : 5	1 : 3.35
1 : 10	1 : 5.98
1 : 50	1 : 11.25

Table S4. The calculated ΔG_{H^*} values for all tested models and sites.

Models and sites	**ΔG_{H^*} (eV)**
Ag_{29}-BDT-H	0.635
Ag_{29}-BDT-T	1.11
Pt_1Ag_{28}-BDT-H	0.606
Pt_1Ag_{28}-BDT-T	1.081
Pt_1Ag_{28}-BTT-H	0.617
Pt_1Ag_{28}-BTT-T	0.986
Pt_1Ag_{28}-BTT-T’	1.287
Pt_1Ag_{28}-BTT-Mn-H	0.616
Pt_1Ag_{28}-BTT-Mn-T	1.096
Pt_1Ag_{28}-BTT-Mn-T’	1.405
Pt_1Ag_{28}-BTT-Mn-Mn	0.186

Table S5. Crystal data and structure refinement for $[Pt_1Ag_{28}(BTT)_{12}(TPP)_2](PPh_4)_4$.

Empirical formula	$Pt_1Ag_{28}S_{36}P_2C_{108}H_{78} + 4(C_{24}H_{20}P)$
Formula weight	7164.72
Temperature/K	120 K
Crystal system	monoclinic
Space group	C2/c
a/Å	31.3153(2)
b/Å	21.4400(2)
c/Å	37.3504(3)
α/°	90
β/°	97.916(10)
γ/°	90
Volume/$Å^3$	24838.1(3)
Z	4
ρcalcg/cm^3	1.916
μ/mm^{-1}	21.799
F(000)	13768.0
Crystal size/mm^3	1 × 1 × 0.2
Radiation	CuK (λ = 1.54186)
Index ranges	-35 ≤ h ≤ 13, -24 ≤ k ≤ 24, -42 ≤ l ≤ 42
2Θ range for data collection/°	9.498 to 124.998
Reflections collected	80478
Independent reflections	90277 [Rint = 0.0473, Rsigma = 0.0331]
Data/restraints/parameters	90277/2028/1125
Goodness-of-fit on F2	1.022
Final R indexes [I>=2σ (I)]	R1 = 0.0838, wR2 = 0.2300
Final R indexes [all data]	R1 = 0.0909, wR2 = 0.2420
Largest diff. peak/hole / e $Å^{-3}$	4.21/-3.58

Reference

1. L. G. AbdulHalim, M. S. Bootharaju, Q. Tang, S. Del Gobbo, R. G. AbdulHalim, M. Eddaoudi, D.-e. Jiang and O. M. Bakr, *J. Am. Chem. Soc.*, 2015, **137**, 11970-11975.

2. M. S. Bootharaju, S. M. Kozlov, Z. Cao, M. Harb, M. R. Parida, M. N. Hedhili, O. F. Mohammed, O. M. Bakr, L. Cavallo and J.-M. Basset, *Nanoscale*, 2017, **9**, 9529-9536.

3. X. Kang, M. Zhou, S. Wang, S. Jin, G. Sun, M. Zhu and R. Jin, *Chem. Sci.*, 2017, **8**, 2581-2587.

4. S. Anantharaj and S. Noda, *J. Mater. Chem. A*, 2022, **10**, 9348-9354.

5. G. Kresse and D. Joubert, *Phys. Rev. B,* 1999, **59**, 1758-1775.

6. G. Kresse and J. Furthmüller, *Phys. Rev. B*, 1996, **54**, 11169-11186.

7. J. P. Perdew, K. Burke and Y. Wang, *Phys. Rev. B*, 1996, **54**, 16533-16539.

8. J. P. Perdew, K. Burke and M. Ernzerhof, *Phys. Rev. Letter*, 1996, **77**, 3865-3868.

9. S. Grimme, J. Antony, S. Ehrlich and H. Krieg, *J. Chem. Phys.*, 2010, **132**, 154104.

10. S. Grimme, S. Ehrlich and L. Goerigk, *J. Comput. Chem.*, 2011, **32**, 1456-65.

11. Y. Li, S. Li, A. V. Nagarajan, Z. Liu, S. Nevins, Y. Song, G. Mpourmpakis and R. Jin, *J. Am. Chem. Soc.*, 2021, **143**, 11102-11108.

12. S. Gratious, A. Karmakar, D. Kumar, S. Kundu, S. Chakraborty and S. Mandal, *Nanoscale*, 2022, **14**, 7919-7926.

13. Y. Du, J. Xiang, K. Ni, Y. Yun, G. Sun, X. Yuan, H. Sheng, Y. Zhu and M. Zhu, *Inorg. Chem. Frontiers*, 2018, **5**, 2948-2954.

14. S. Zhao, R. Jin, Y. Song, H. Zhang, S. D. House, J. C. Yang and R. Jin, *Small*, 2017, **13**, 1701519..

15. M. Ghosal Chowdhury, L. Sahoo, S. Maity, D. Bain, U. K. Gautam and A. Patra, *ACS Appl. Nano Mater.*, 2022, **5**, 7132-7141.

16. X. Cheng, Y. Li, L. Zheng, Y. Yan, Y. Zhang, G. Chen, S. Sun and J. Zhang, *Energy Environ. Sci.*, 2017, **10**, 2450-2458.

17. B. Jiang, Y. Sun, F. Liao, W. Shen, H. Lin, H. Wang and M. Shao, *J. Mater. Chem. A*, 2017, **5**, 1623-1628.

18. R. Nazir, P. Fageria, M. Basu and S. Pande, *The J. Phy. Chem. C*, 2017, **121**, 19548-19558.

19. Y. Jo, M. Choi, M. Kim, J. S. Yoo, W. Choi and D. Lee, *Bull. Korean Chem. Soc.*, 2021, **42**, 1672-1677.

20. Y. Chen, X. Zeng, Y. Liu, R. Ye, Q. Liang and J. Hu, *Chem. Commun.*, 2021, **57**, 9410-9413.